Applied Physics A (2021) 127:745
https://doi.org/10.1007/s00339-021-04896-w

Applied Physics A
Materials Science & Processing

Oxygen defect related high temperature dielectric relaxation behavior in (Ba,La)(Zr,Sn,Ti)O_3 ceramics

Ke Meng[1] · Wenhua Li[1] · Xingui Tang[1] · Xiaobin Guo[1] · Qiuxiang Liu[1] · Yanping Jiang[1]

Received: 13 July 2021 / Accepted: 31 August 2021 / Published online: 7 September 2021

Abstract
Ferroelectric materials with the typical perovskite structure are widely used in capacitors, ultrasonic devices, oil drilling, transducers, and other fields. Lead-lanthanum-zirconium-titanate ceramics co-doped with *Sn* and *Ba*, have been widely investigated. However, there is little attention has been focused on the dielectric properties of barium-lanthanum-zirconium-titanate. Thus, in this work, *Sn* doped $Ba_{0.955}La_{0.03}Zr_{0.02}Ti_{0.98}O_3$ ferroelectric ceramics were prepared via a classical high-temperature solid state reaction. Scanning Electron Microscopy (SEM) was used to observe the surface appearance of ceramics. The X-ray diffraction (XRD) patterns at room temperature, indicate that the ceramics are well crystallized. Impedance properties and dielectric properties reflect the characteristic of typical high temperature dielectric relaxation behavior. The conductive activation energy and the relaxation activation energy are obtained through the calculation of the Arrhenius law. The fitting results show that the dielectric relaxation behavior at high-temperature, was related to the oxygen defect. The electrical modulus verified the partial short-range carrier migration, also contribute to the high-temperature dielectric properties.

Keywords Dielectric relaxation · Oxygen defect · Ferroelectric · Electrical modulus

1 Introduction

Since the discovery of ferroelectricity in barium titanate in 1940, it has been widely used in certain electronic industries, ranging from the sonar in World War II to later piezoelectric actuators, and transducers [1]. $BaTiO_3$ owns a high dielectric constant, and low dielectric loss tangent [2, 3]. It presents four different phases structure from low temperature to their melt point. The adjustment of the Curie point could help the practical application of it. The substitution of La^{3+} ion for Ba^{2+} ion also depresses the Curie temperature in $BaTiO_3$. It shows a high dielectric constant, high insulation resistance, and long service life [4]. Since the doping of Zr^{4+} ion will affect the phase structure of $BaTiO_3$, the permittivity of $BaTi_{1-x}Zr_xO_3$ is intensively affected by the ratio of *Zr*/*Ti*. With the increasing content of *Zr*, the average grain size and premittivity decreased [5]. The doping of Sn^{4+} ion could depress the value of Curie temperature, and it formed a relaxor ferroelectric with the adding of it [6]. Usually, space charge, Maxwell-Wanger polarization, interfacial polarization could arouse the relaxor phenomenon [7]. Smolensky et al. attributed the relaxor phenomenon in $BaTi_{1-x}Sn_xO_3$ (x is the content of doping) to the polar nano regions [8]. As we all know, the relaxor ferroelectric has a slim hysteresis loop, while the antiferroelectric has a specifitic double hysteresis loop. Both of them have potential in the application of dielectric energy-storage devices. The lead-lanthanum-zirconium-titanate (PLZT), as an antiferroelectric, has been widely studied in the application of energy storage [9–11]. Because of the similar ionic radii between Ba^{2+} (1.61 Å) and Pb^{2+}(1.49 Å), Ba^{2+} ion doped PLZT ceramics also have been prepared to study their dielectric properties [12–16]. Although there are some articles focusing on Sn^{4+} doped PLZT, there are almost no reports on the dielectric properties and impedance properties of $(Ba,La)(Zr,Ti,Sn)O_3$ ceramics. Our previous article has studied the dielectric properties of non-stoichiometry $(Ba,La)(Ti,Sn)O_3$ ferroelectric ceramics [17]. There might be a difference in the dielectric properties between the non-stoichiometry and the stoichiometry. In addition, relaxor ferroelectric ceramics have been widely used in the application of energy storage. The study of the relaxation behavior of $(Ba,La)(Zr,Ti,Sn)O_3$ might provide

✉ Wenhua Li
liwenhuat@gdut.edu.cn

[1] Guangzhou Higher Education Mega Center, School of Physics and Optoelectronic Engineering, Guangdong University of Technology, Guangzhou 510006, China

another dielectric material for ferroelectric capacitors. Thus, this article focuses on the dielectric properties and impedance properties of these ferroelectric ceramics.

2 Experimental

The traditional solid-state sintering method was used to prepare lead free $Ba_{0.955}La_{0.03}Zr_{0.02}Ti_{0.98}O_3$ (BLZST0), $Ba_{0.955}La_{0.03}Zr_{0.02}Ti_{0.97}Sn_{0.01}O_3$ (BLZST1), $Ba_{0.955}La_{0.03}Zr_{0.02}Ti_{0.96}Sn_{0.02}O_3$ (BLZST2), $Ba_{0.955}La_{0.03}Zr_{0.02}Ti_{0.95}Sn_{0.03}O_3$ (BLZST3) ceramics. First, initial raw materials $BaCO_3$ (99%) and SnO_2 (99.5%) (Aladdin Reagent Co. Ltd, China), TiO_2 (99%) (DAMAO CHEMICAL REAGENT FACTORY, China), La_2O_3 (99.9%), and ZrO_2 (99%) (Shanghai Maclin Biochemical Co. Ltd, China), were weighted according the chemical stoichiometry ratio. Second, these initial raw materials were put into a container and balling milled with ethanol for 8 h. Different sizes (0.5, 1, 3, 5 mm) of zirconia ball milling beads were used for ball milling. The weight ratios of different beads keep 1:1:1:1. Since the weight of a small ball is light, the number of small balls is the biggest, while the number of big balls is the least. However, the total weight of ball milling beads: the weight of raw materials: the weight of ethanol = 2: 1: 0.6. The total volumes of beads, initial raw materials, and ethanol should cover 40–60% of the total volume of nylon can. Then, these slurries were poured into beakers and drying at 373 K for 24 h. After these slurries had been dried, we put them in the corundum crucible, and these initial raw materials were calcined in the muffle furnace at 1373 K for 4 h. The calcined materials, were reground and dried again. The Polyvinyl butyral (PVB) was used for granulation. These particles were pressed into a disk shape module with pressure. Then, these ceramics were sintered at 1673 K for 290 min. The heating rate and cooling rate, should not be so fast. The heating rate ranges from 2 to 3 °C, and the cooling rate ranges from 1 to 2 °C. The specific preparation process is shown in Fig. 1. Sandpapers were used to polish the surface of the ceramics. Paste the silver electrode on the ceramic to test the high-temperature dielectric properties and impedance properties of ceramics. The precision LCR (E4980A, Agilent, USA) meter was used to measure the relative dielectric constant, the loss tangent, and the impedance properties. The crystal structure of ceramics, was analyzed by X-ray diffraction (D8 ADVANCE, German, Bruker). The scanning electron microscope (SU8220, Hitachi, Japan) is used to observe the surface appearance of ceramics. X-ray photoelectron spectroscopy (XPS) (Escalab 250Xi, Thermo Fisher, UK) is used to analyze the oxygen vacancies.

3 Results and discussion

The X-ray diffraction patterns of polycrystalline ceramic pellets were shown in Fig. 2. As shown in Fig. 2b, the diffraction peaks shifted to a lower angle. This phenomenon is the result of the doping of tin. As we all know, the *X*-ray diffraction patterns obey the Bragg's law:

$$2D\sin\theta = k\lambda \tag{1}$$

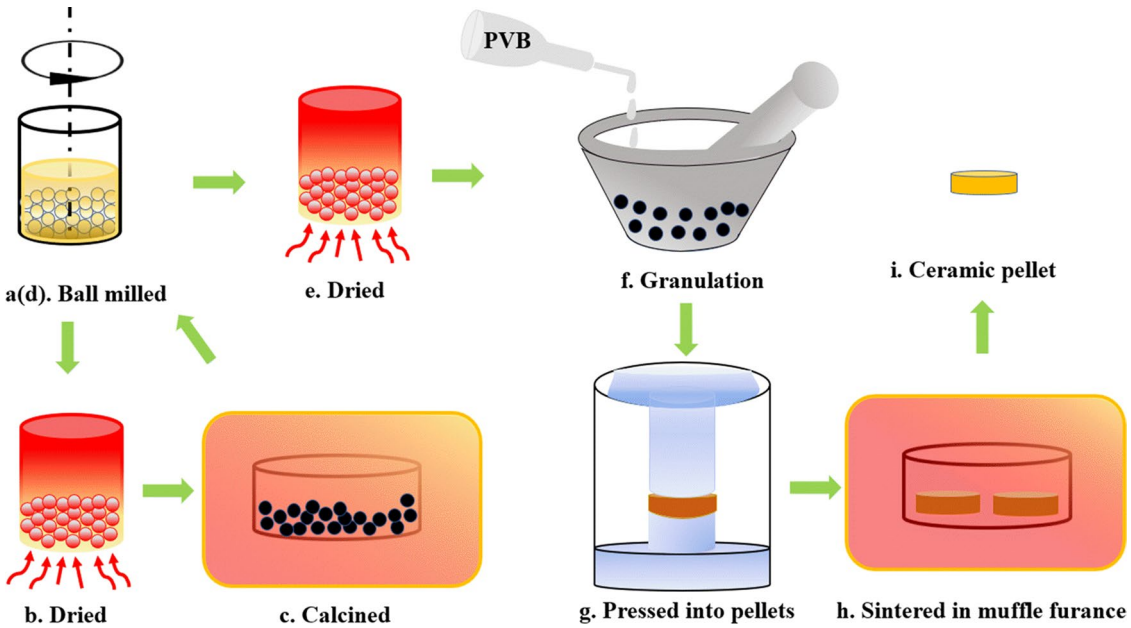

Fig. 1 The preparation process of ceramic pellet

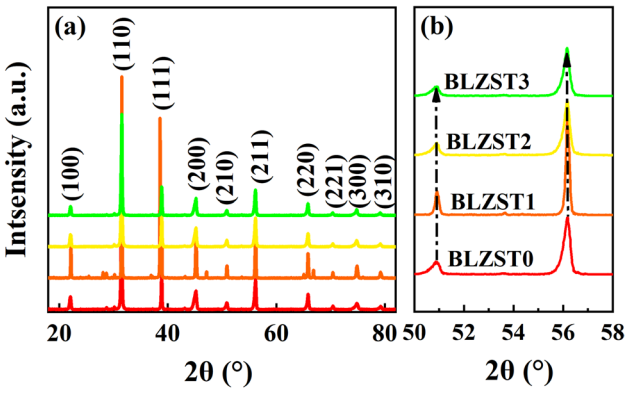

Fig. 2 The XRD patterns of ceramics at room temperature

Table 1 The lattice parameters (*a*, *b*, *c*, Volume) of BLZST0, BLZST1, BLZST2, and BLZST3 ferroelectric ceramics

Samples	*a* (Å)	*b* (Å)	*c* (Å)	Volume (Å^3)
BLZST0	4.00756	4.00756	4.00304	64.2910
BLZST1	4.00711	4.00711	4.00759	64.3497
BLZST2	4.00769	4.00769	4.00513	64.3286
BLZST3	4.00765	4.00765	4.00544	64.3324

D is the grating space; θ is the diffraction angle; λ is the wavelength of the *X*-ray; *k* is a constant. Since for the larger ion radius of Sn^{4+}(0.69 Å) than Ti^{4+}(0.605 Å), all of these diffraction peaks shifted to a lower angle, when the Ti^{4+} ion are substituted for Sn^{4+} ion [12]. These results also proves that the Sn^{4+} ion has substituted for the Ti^{4+} ion indeed. Table 1 is the lattice parameters obtained by UnitCell software of these ceramics. With the doping of Sn^{4+} ion, the volume of the unit cell presents an increasing tendency. This also confirms the Sn^{4+} ion substitution for Ti^{4+} ion in this system.

Figure 3 is the SEM of the surface of ceramics. Few pores were observed in these ceramics, demonstrating their good compactness. In addition, the Archimedes' drainage method was used to measure the density of these ceramics. The density of BLZST0, BLZST1, BLZST2, and BLZST3 is 5.938, 5.742, 5.851, 5.773 g/cm^3, separately. The inset of Fig. 3 is average grain size of these ceramics. The average grain size for BLZST0, BLZST1, BLZST2, and BLZST3 is 0.897, 0.911, 1.411, and 1.127 μm, respectively.

Figure 4 is the relative permittivity and loss tangent of ceramics. The value of relative permittivity, firstly increases, and then decreases. This phenomenon is related to the size of crystal grain [18]. The noticeable anomalies near the starting point in Fig. 4 are attributed to the transition of the ferroelectric tetragonal phase to the paraelectric phase. Since the different polarization mechanisms, such as electron polarization and orientation polarization, has different response frequencies. These different polarization types also affect to the value of permittivity. Thus, the permittivity is frequency related. There is a shoulder peak around the 400–600 °C. With the increase of frequency, the shoulder peak moves to a higher temperature, marked by a black arrow. This phenomenon is the typical relaxation behavior [19]. Similar behaviors also appear in the dielectric dissipation factor. The reason why 1 kHz data is more evident, is because of the fact that ionic contribution can be monitored at this particular frequency, as it responds well under 1 kHz. It is well known that the relaxation phenomenon might result from the following reasons: Maxwell-Wanger polarization, space-charge polarization, interfacial polarization, and dipolar polarization. The Maxwell-Wanger model is suitable for explaining the relaxation phenomenon, with remarkably high permittivity. This model is not suitable for our experimental phenomenon. In addition, the dipolar relaxation frequency, usually appears microwave-frequency (300 MHz–3000 GHz) or radio-frequency. Nonetheless, the relaxation frequency in Fig. 4 is between 100 Hz and1 MHz, which is mainly controlled by defect chemistry. Since the sintering temperature is bigger than 1350 °C, the oxygen in the air atmosphere will be ionized at 1350 °C. The specific formation procedure is as follows [20]:

$$V_O \leftrightarrow V_{\dot{O}} + e'$$

$$V_{\dot{O}} \leftrightarrow V_{\ddot{O}} + e'$$

As we all know, the hole and electron can be treated as the charge carriers. The oxygen vacancies belong to the hole. When the decrease of temperature, the random distribution of oxygen vacancies in ceramics will form the space charge. However, as the temperature increases, these oxygen vacancies are thermally activated [21–23]. Thus, this unusual high-temperature dielectric relaxation might attribute to space-charge-related oxygen defect [7, 24]. Oxygen vacancies associated conduction behavior might affect the dielectric properties, with the increase of frequency and temperature. Similarly, more bounded charge carriers could get enough energy to cross the energy barrier, as temperature increases. This also explained the big loss tangent at high-temperature. Relaxor ferroelectric ceramics are widely used in the application of energy storage. Fig. S1 and Fig. S2, are the ferroelectric hysteresis loops and energy storage density, respectively. Fig. S2 shows that the BLZST1 has better relaxation properties for energy storage applications.

The impedance spectroscopy provides us another method to analyze the relaxation behavior. Figure 5 is the Cole–Cole diagram of ceramics. One clear curve appears in these images. With the increase in temperature, these curves

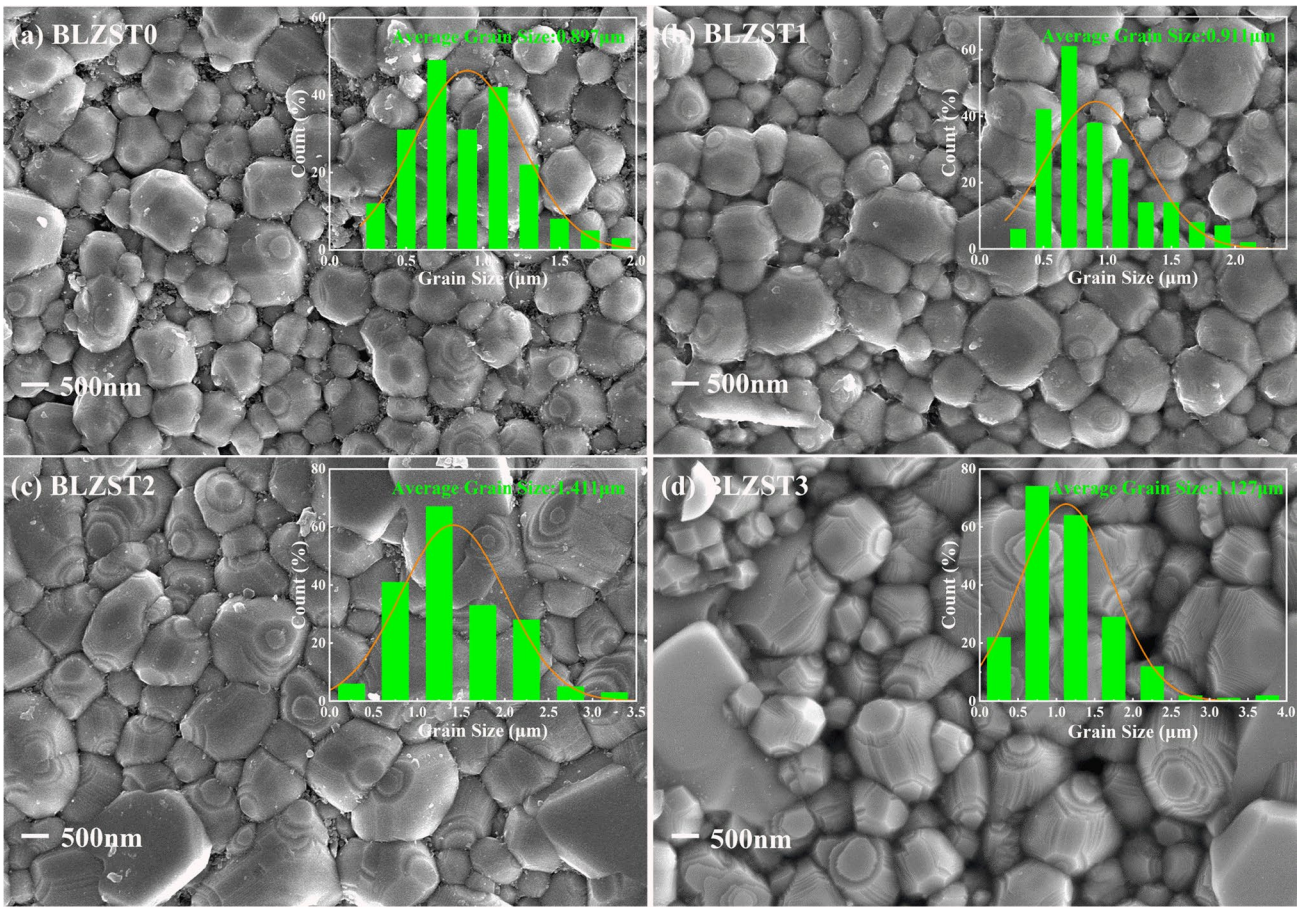

Fig. 3 The surface SEM images of ceramics

get smaller. This behavior can be explained as follows: the space charges are easier to migrate at high temperatures, and these charges gain enough energy to jump the energy barrier. Thus, the radius of the curve gets smaller [20]. What's more, these curves obviously deviated from the ideal Debye relaxation (the center of the semicircles lies on a line below the real axis). Figure 5e is the fitting results of the impedance spectroscopy. The semicircle curve in the ideal Nyquist plot, can be replaced by the parallel of resistor and capacitor. However, our experimental results deviate the ideal model. Thus, it can be replaced by the parallel of constant phase element (CPE) and resistor. The equivalent circuit shows the contribution of grain and grain boundary to the impedance [25–27]. Due to the effect of the electrode, the starting point of the curve is not zero [28]. The inset of Fig. 5 is the normalized impedance imaginary part. One obvious peak appears in it, and these peaks move to a higher frequency, along with the increase of temperature. This phenomenon presents the typical thermal activation behavior, and it is exemplary of trap hopping.

According to the Arrhenius equation, the activation energy (E_a) and conductive activation energy (E_c) shows as follows [6, 21]:

$$\tau = \tau_0 \exp(E_a/k_\beta T) \tag{2}$$

$$\sigma_{\mathrm{AC}} = \sigma_0 \exp(-E_c/k_\beta T) \tag{3}$$

The τ is the relaxation time; The τ_0 is the relaxation time, when the temperature is infinite. The k_β is the Boltzmann constant; The T is the absolute temperature. The $\omega_p\tau_p$ equals one at the peak of the normalized impedance imaginary part. The alternate current conductivity of samples can be calculated by the following equation: $\sigma_{AC}=\omega\varepsilon_0\varepsilon''$. ω is the angular frequency, and their value can be calculated by $\omega=2\pi f$. The f is test frequency. The ε_0 is the vacuum dielectric constant. The ε'' is the imaginary part of complex dielectric constant, and it equals to $\varepsilon''=\varepsilon_r tan\delta$. The value of E_a and E_c is obtained by the linear fitting. Fig. 6 is the calculation of the E_a and E_c. The fitting results were presented in Table 2. These results meet the previous report related to the oxygen

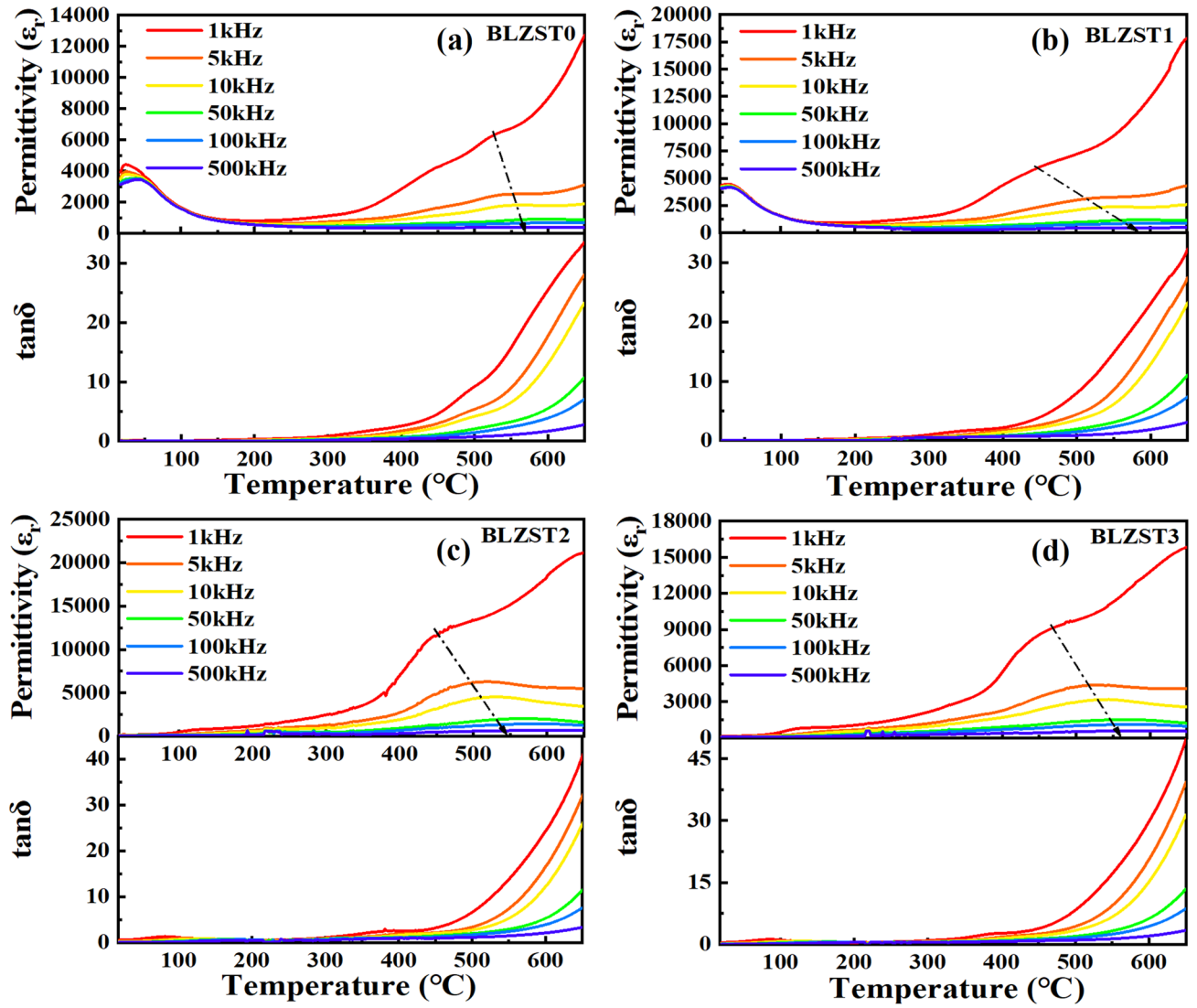

Fig. 4 The relative permittivity (ε_r) and the loss tangent (tan δ) of ceramics from 18 to 650 °C

vacancies [7]. Ideally, the value of E_a for a typical ABO_3 perovskite structure is 2.0 eV. Because of the concentration degree of oxygen vacancies is different, the value of E_a is different from others. However, the value of E_a for stoichiometric $ABO_{2.8}$, $ABO_{2.9}$, and $ABO_{2.95}$ is 0 eV, 0.5 eV, and 1 eV, respectively [29]. Thus, the values of E_a and E_c indicate that the high-temperature relaxation behavior is mainly caused by oxygen vacancies [17, 30].

Furthermore, complex electrical modulus is a good tool to analyze dielectric behavior. The complex electrical modulus and the Nyquist plot describe impedance from the perspective of capacitance and resistance, respectively. The complex modulus (M^*) can be obtained through the following equation [31]:

$$M^* = M' + jM'' = \frac{1}{\varepsilon^*} \tag{4}$$

ε^* is the complex dielectric constant; M' and M'' is the real and imaginary part complex electrical modulus, respectively $j = \sqrt{-1}$. In addition, the complex electrical modulus also can be expressed as the equation of complex impedance (Z^*=Z'+jZ'').

$$M^* = j\omega\varepsilon_0 Z^* = j\omega\varepsilon_0 Z' - \omega\varepsilon_0 Z'' \tag{5}$$

Thus, according to Eqs. (4) and (5), the imaginary part of complex electrical modulus can be expressed as follows [28, 32, 33]:

$$M'' = 2\pi f C_0 Z' \tag{6}$$

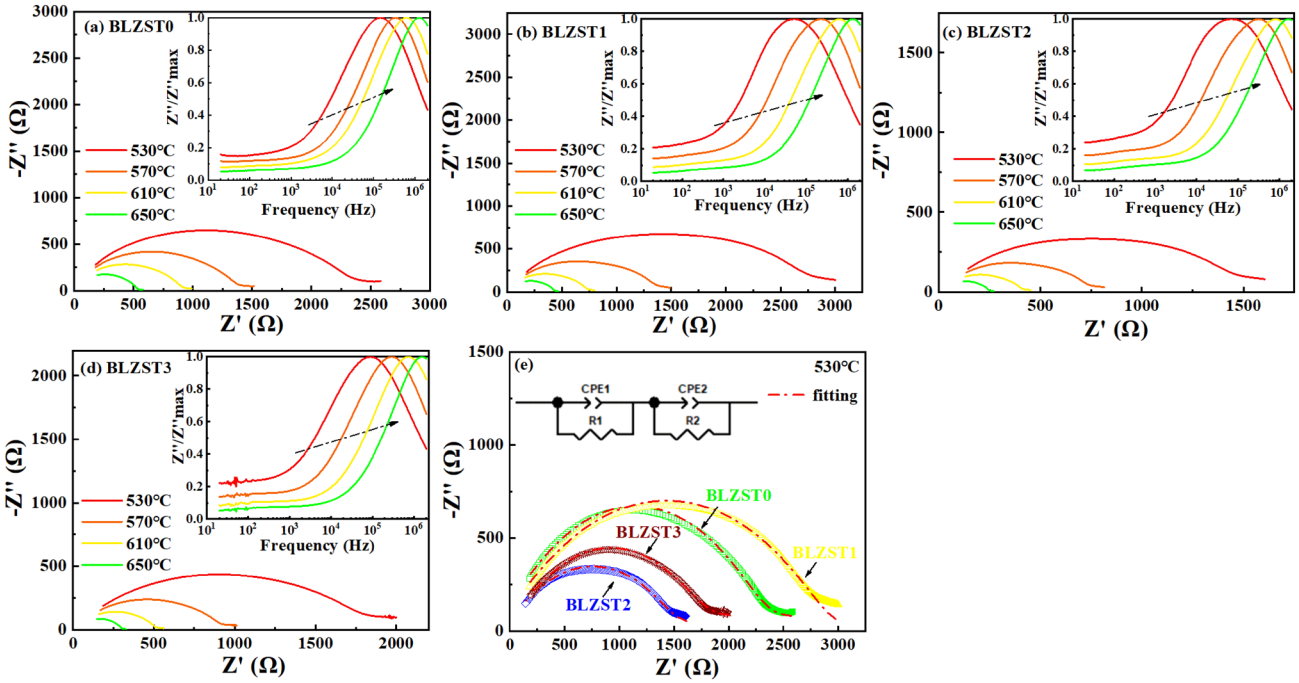

Fig. 5 **a**–**d** The impedance spectroscopy of these ceramics (the inset is the normalized impedance imaginary part. **e** The fitting results of the Nyquist plot at 530 °C (the inset is the equivalent circuit of impedance spectroscopy)

Table 2 The values of relaxation activation energy and conductive activation energy by fitting the Arrhenius law

Sample	E_a/eV	E_c/eV
BLZST0	1.12	0.90
BLZST1	1.77	0.96
BLZST2	1.67	0.93
BLZST3	1.50	0.92

C_0 is the vacuum permittivity (vacuum capacitance); f is frequency; The plot of Z'' and M'' under different frequencies are shown in Fig. 7. There is only one peak that appears in the Frequency-Z'' plot. This peak is attributed to the contribution of grain [34]. There is a difference between the resistance of grain and grain boundary. If the size of the grain

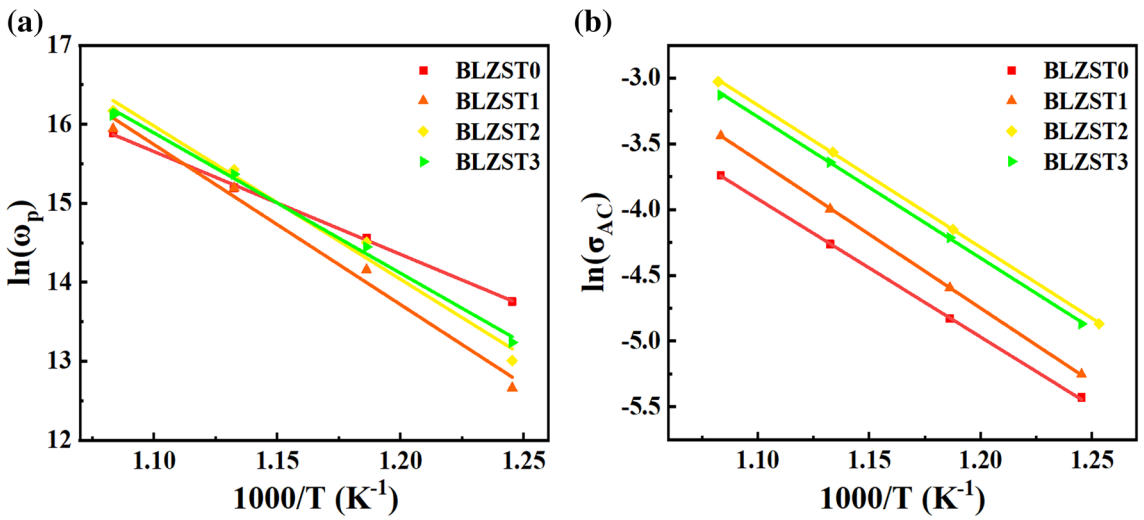

Fig. 6 The calculation of the **a** relaxation activation energy and **b** conductive activation energy

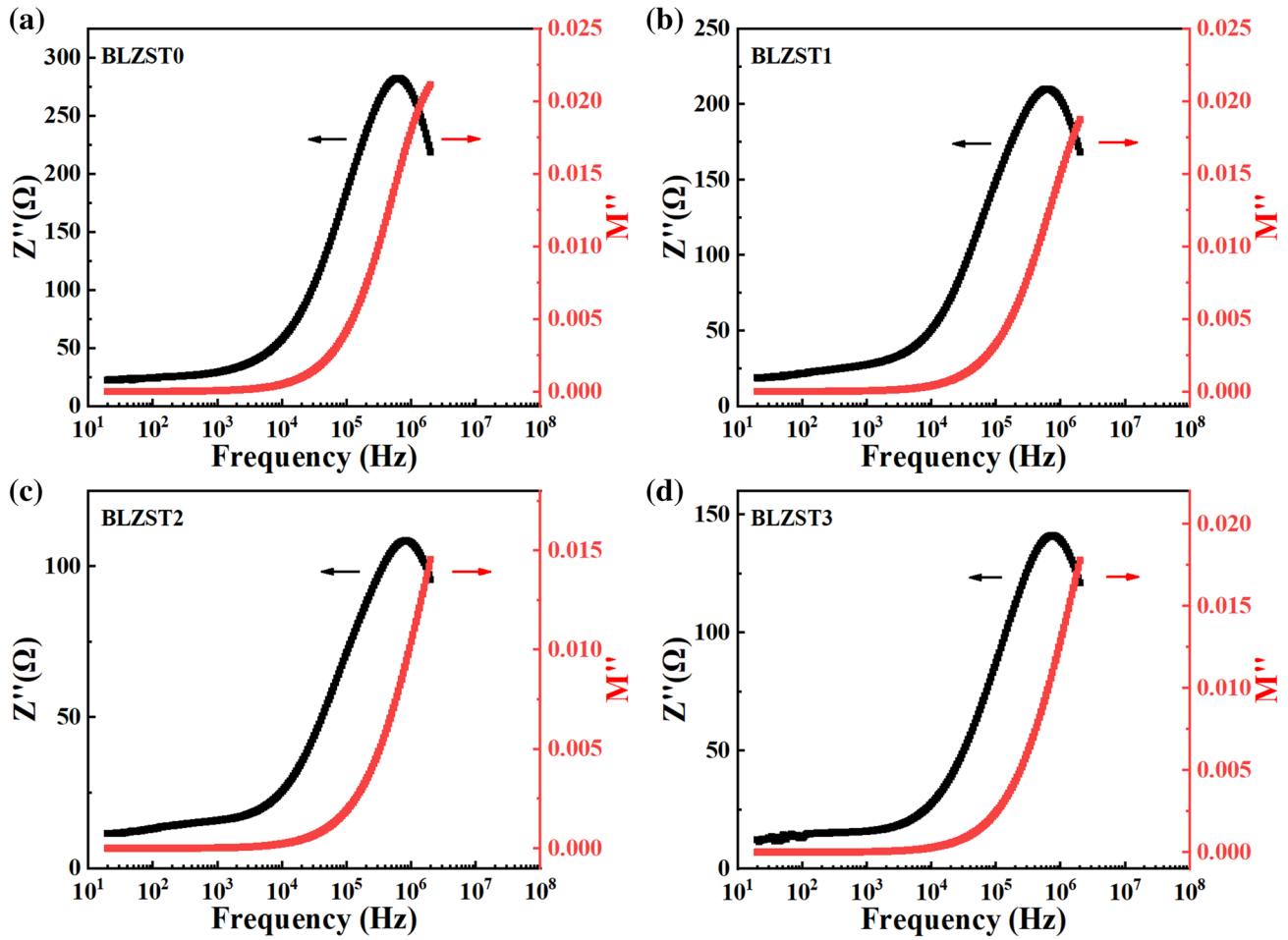

Fig. 7 The imaginary part of impedance (Z'') and electrical modulus (M'') with different frequencies of ceramics

is big, the area of the grain boundary is small. Thus, the grain boundary has little effect on the scattering of electrons. Finally, it shows a small impedance. However, if the size of the grain is small, the grain boundary has a large effect on the scattering of electrons, and it shows a large impedance [35]. Unfortunately, due to the limitation of the testing frequency range, no peak has been found in the Frequency-M'' plot. There is just a curve with an increasing trend. The mismatch of the peak between Frequency-Z'' and Frequency-M'' shows that partial short-range carrier migration also donates the dielectric response behavior [36–39].

The XPS or the Raman spectroscopy could study the behavior of oxygen vacancies. Figure 8 is the XPS of these ceramics. The asymmetric broadening of the O1s peak close to 531 eV is due to the existence of oxygen vacancies. These asymmetric curves can be fitted by three symmetrical peaks. These low binding energy peaks (near 529 eV) are attributed to the O^{2-} ions, surrounded by metal atoms. These high binding energy peaks (near 531 eV) are attributed to the oxygen vacancies. These mid-binding energy peaks were attributed to the absorbed oxygen [40, 41].

4 Conclusions

The commercial solid-state reaction method was used to prepare ferroelectric ceramics. The high-temperature dielectric behaviors and impedance properties of *Sn* doped $Ba_{0.955}La_{0.03}Zr_{0.02}Ti_{0.98}O_3$ ceramics, were firstly studied in this article. The dielectric properties show a typical relaxation behavior. According to the fitting results of E_a and E_c, this dielectric relaxation behavior is mainly attributed to the effect of oxygen vacancies. The XPS results of these ceramics confirm the existence of oxygen vacancies. The electrical modulus, also verified the effect of migration of carriers to the dielectric properties.

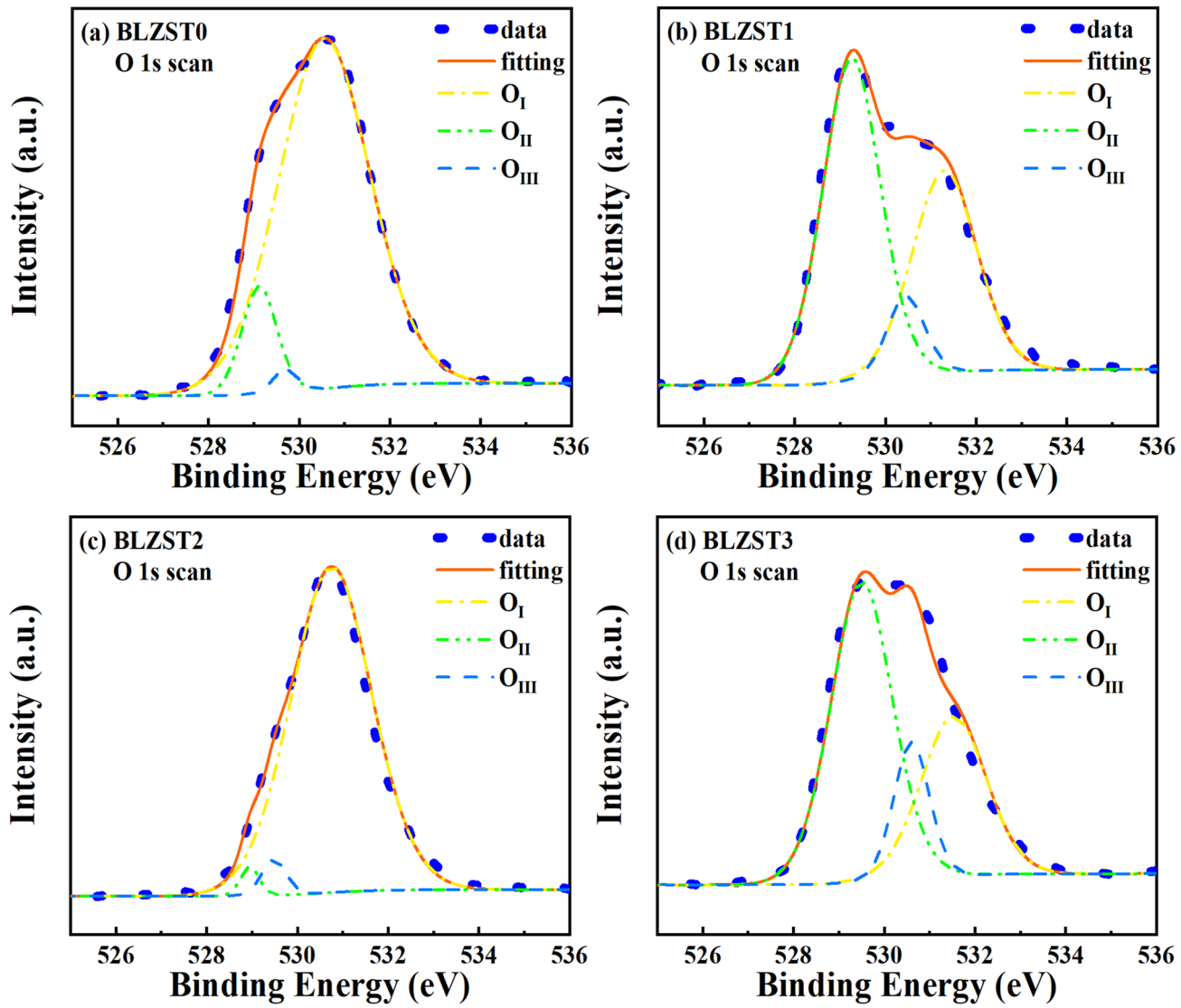

Fig. 8 The XPS results of O1s for these ceramics with different content of *Sn*

Supplementary Information The online version contains supplementary material available at https://doi.org/10.1007/s00339-021-04896-w.

Acknowledgements This work was supported by the National Natural Science Foundation of China (Grant Nos. 51604087, 11574057, 11904056), the Guangdong Provincial Natural Science Foundation of China (Grant No. 2016A030313718), and the Science and Technology Program of Guangdong Province of China (Grant Nos. 2017A010104022).

Declarations

Conflict of interest The authors have no relevant financial or non-financial interests to disclose.

References

1. G.H. Haertling, J. Am. Ceram. Soc. **82**, 797–818 (1999)
2. L.W. Wu, X.H. Wang, H.L. Gong, Y.N. Hao, Z.B. Shen, L.T. Li, J. Mater. Chem. C **3**, 750–758 (2015)
3. R. Kumar, K. Asokan, S. Patnaik, B. Birajdar, J. Alloy. Compd. **737**, 561–567 (2018)
4. M. Gangly, S.K. Rout, T.P. Sinha, S.K. Sharma, H.Y. Park, C.W. Ahn, I.W. Kim, J. Alloys Compd. **579**, 473–484 (2013)
5. F. Moura, A.Z. Simões, B.D. Stojanovic, M.A. Zaghete, E. Longo, J.A. Varela, J. Alloys Compd. **462**, 129–134 (2008)
6. L. Zhao, X. Wei, IEEE Trans. Dielectr. Electr. Insul. **22**, 728–733 (2015)
7. C. Elissalde, J. Ravez, J. Mater. Chem. **11**, 1957–1967 (2001)
8. X.Y. Wei, Y.J. Feng, X. Yao, Appl. Phys. Lett. **83**, 2031–2033 (2003)
9. R. Xu, Z. Xu, Y.J. Feng, J.J. Tian, D, Huang. Ceram. Int. **42**, 12875–12879 (2016)

10. Y.Q. Li, W.P. Geng, L. Zhang, X.Y. Yang, X.J. Qiao, D.W. Zheng, L.Y. Zhang, J. He, X.J. Hou, X.J. Chou, J. Alloy. Compd. **868**, 159129 (2021)
11. Y. Yang, P. Liu, Y.J. Zhang, K.R. Kandula, J.W. Xu, G.Z. Zhang, Ceram. Int. **46**, 18106–18113 (2020)
12. R.D. Shannon, Acta Crystallogr. Sect. A **32**, 751–767 (1976)
13. X.C. Wang, W.Q. Cai, Z. Xiao, X.M. Yu, J.W. Chen, T.Q. Yang, J. Mater. Sci. Mater. Electron. **31**, 17013–17017 (2020)
14. Q.F. Zhang, S.L. Jiang, Y.K. Zeng, J. Mater. Res. **26**, 1436–1440 (2011)
15. Q. Zhang, X.L. Liu, Y. Zhang, X.Z. Song, J. Zhu, I. Baturin, J.F. Chen, Ceram. Int. **41**, 3030–3035 (2015)
16. B.L. Peng, S.L. Tang, L. Lu, Q. Zhang, H.T. Huang, G. Bai, L. Miao, B.S. Zou, L.J. Liu, W.H. Sun, Z.L. Wang, Nano Energy **77**, 105132 (2020)
17. K. Meng, W.H. Li, X.G. Tang, Q.X. Liu, Y.P. Jiang, Appl. Phys. A **127**, 337 (2021)
18. G. Arlt, D. Hennings, G.D. With, J. Appl. Phys. **58**, 1619–1625 (1985)
19. M. Peddigari, H. Palneedi, G.T. Hwang, K.W. Lim, G.Y. Kim, D.Y. Jeong, J.G. Ryu, A.C.S. Appl, Mater. Interfaces **10**, 20720–20727 (2018)
20. J. Wei, T.Q. Yang, H.S. Wang, J. Eur. Ceram. Soc. **39**, 624–630 (2019)
21. L.N. Liu, C.C. Wang, X.H. Sun, G.J. Wang, C.M. Lei, T. Li, J. Alloy. Compd. **552**, 279–282 (2013)
22. N. Zhang, Q.J. Li, S.G. Huang, Y. Yu, J. Zheng, C. Cheng, C.C. Wang, J. Alloy. Compd. **652**, 1–8 (2015)
23. G. Singh, V.S. Tiwari, P.K. Gupta, J. Appl. Phys. **107**, 064103 (2010)
24. O. Bidault, P. Goux, M. Kchikech, M. Belkaoumi, M. Maglione, Phys. Rev. B **49**, 7868 (1994)
25. V. Senthi, T. Badapanda, S.N. Kumar, P. Kumar, S. Panigrahi, J. Polym. Res. **19**, 9838 (2012)
26. S. Pattanayak, B.N. Parida, P.R. Das, R.N.P. Choudhary, Appl. Phys. A **112**, 387–395 (2013)
27. S. Dash, R.N.P. Choudhary, A. Kumar, J. Phys. Chem. Solids **75**, 1376–1382 (2014)
28. T.S.I. John, C.S. Derek, R.W. Anthony, Adv. Mater. **2**, 132–138 (1990)
29. J.F. Scott, M. Dawber, Appl. Phys. Lett. **76**, 3801–3803 (2000)
30. J. Miao, X.G. Xu, Y. Jiang, L.X. Cao, B.R. Zhao, Appl. Phys. Lett. **95**, 132905 (2009)
31. M. Coskun, Ö. Polat, F.M. Coskun, Z. Durmus, M. Cağlar, A. Türüt, RSC Adv. **8**, 4634 (2018)
32. R. Mouss, A. Bougoffa, A. Trabelsi, E. Dhahri, M.P.F. Graca, M.A. Valente, R. Barille, J. Mater. Sci. Mater. Electron. **32**, 11453–11466 (2021)
33. A. Singh, K. Prasad, A. Prasad, Process. Appl. Ceram. **9**, 33–42 (2015)
34. J. Kolte, P.H. Salame, A.S. Daryapurkar, P. Gopalan, AIP Adv. **5**, 097164 (2015)
35. K. Sangtae, Monatsh. Chem. **140**, 1053–1057 (2009)
36. R. Panigrahi, S. Hajra, M. De, A. Kumar, A.R. James, R.N.P. Choudhary, Solid State Sci. **92**, 6–12 (2019)
37. Q.L. Li, J.W. Liu, D.Y. Lu, W.T. Zheng, Ceram. Int. **44**, 7251–7258 (2018)
38. F.I.H. Rhouma, A. Dhahri, J. Dhahri, M.A. Valente, Appl. Phys. A **108**, 593–600 (2012)
39. S.N. Das, S.K. Pradhan, S. Bhuyan, R.N.P. Choudhary, J. Mater. Sci. Mater. Electron. **28**, 18913–18928 (2017)
40. L. Aswaghosh, D. Manoharan, N.C. Jaya, Phys. Chem. Chem. Phys. **8**, 5995–6004 (2016)
41. M. Chen, Z.L. Pei, C. Sun, L.S. Wen, X. Wang, Mater. Lett. **48**, 194–198 (2001)